

Tuneable Nonlinear Spin Response in a Nonmagnetic Semiconductor

Y.Q. Huang^{1,*†}, V. Polojärvi,² A. Aho,² R. Isoaho,² T. Hakkarainen,² M. Guina,² I.A. Buyanova¹,[‡] and W.M. Chen¹

¹Department of Physics, Chemistry and Biology, Linköping University, Linköping S-581 83, Sweden

²Optoelectronics Research Centre, Physics Unit, Tampere University, Korkeakoulunkatu 3, Tampere 33800, Finland



(Received 2 February 2023; revised 12 April 2023; accepted 18 May 2023; published 15 June 2023)

Nonlinear effects and dynamics are found in a wide range of research fields. In magnetic materials, nonlinear spin dynamics enables ultrafast manipulation of spin, which promises high-speed nonvolatile information processing and storage for future spintronic applications. However, a nonlinear spin response is not yet demonstrated in a nonmagnetic material that lacks strong magnetic interactions. Dilute nitride III-V materials, e.g., (Ga, N)As, have the ability to amplify the conduction-electron-spin polarization by filtering out minority spins via spin-polarized defect states at room temperature. Here, by employing coupled rate equations, we theoretically demonstrate the emergence of a nonlinear spin response in such a defect-enabled room-temperature spin amplifier. Furthermore, we showcase the proposed spin nonlinearity in a (Ga, N)As-InAs quantum dot (QD) coupled all-semiconductor nanostructure, by measuring the higher-harmonic generation, which converts the modulation of excitation polarization into the second-, third-, and fourth-order harmonic oscillations of the QD's photoluminescence intensity and polarization. The observed spin nonlinearity originates from defect-mediated spin-dependent recombination, which can be conveniently tuned with an external magnetic field and can potentially operate at a speed exceeding 1 GHz. The demonstrated spin nonlinearity could pave the way for nonlinear spintronic and optospintronic device applications based on nonmagnetic semiconductors with simultaneously achievable high operation speed and nonlinear response.

DOI: 10.1103/PhysRevApplied.19.064048

I. INTRODUCTION

Systems with strong nonlinearity can give rise to complex behaviors that are not only of fundamental scientific interest but may also lead to practical applications beyond the capability of a linear system. Nonlinear effects are widely explored in a variety of research fields, including nonlinear optics [1–5], electric transport [6–8], and spin dynamics [9–14]. Nonlinear phenomena, such as frequency conversion and harmonic generation, find applications in creating coherent light sources of new colors [1,4]. In magnetic materials, nonlinear spin dynamics is shown to be an important candidate for terahertz light sources [13,14]. Moreover, nonlinear spin dynamics in magnetic

materials and devices enables ultrafast magnetic switching, which promises high-speed nonvolatile information processing and storage for future applications in spintronics and quantum information technology [13,15]. However, such nonlinear spin dynamics, so far, is only considered in magnetic materials with strong enough interactions (such as strong exchange) or in nonmagnetic materials with strong spin-orbit coupling [15–17]. In nonmagnetic semiconductors that are the backbone of today's electronics and photonics, such spin nonlinearity is generally absent, which imposes constraints on harnessing their full potential for future spintronic applications.

Recently, efficient defect-enabled spin amplification was demonstrated at room temperature in (Ga, N)As-based semiconductor nanostructures [18,19]. By taking advantage of spin-dependent recombination via a defect state, such a room-temperature spin amplifier enables alternative visions for semiconductor spintronics and the spin-photon interface at a practical operation temperature. In previous studies, the nonlinear nature of the spin-amplification process was largely overlooked. Exploring the nonlinear effect in the room-temperature spin amplifier can therefore not only fill the gap in the ongoing pursuit of nonlinear spin physics in a nonmagnetic material, but also it could

*yqhuang@semi.ac.cn

†Present address: State Key Laboratory of Superlattices and Microstructures, Institute of Semiconductors, Chinese Academy of Sciences, Beijing, China

Published by the American Physical Society under the terms of the Creative Commons Attribution 4.0 International license. Further distribution of this work must maintain attribution to the author(s) and the published article's title, journal citation, and DOI. Funded by Bibsam.

pave the way to create room-temperature-operational semiconductor spintronic devices, which are a major challenge in the research field.

Here, we demonstrate the nonlinear response of a room-temperature defect-enabled spin amplifier by measuring the harmonic generation from a periodic modulation of the conduction-electron spin polarization in an all-semiconductor nanostructure consisting of tunneling-coupled (Ga, N)As and InAs quantum dots (QDs). We show that the spin nonlinearity is derived from the spin-dependent recombination mediated by defect states and can be conveniently tuned with a small external magnetic field. Such a tunable nonlinear spin response can readily operate at a frequency exceeding 1 GHz and does not require the strong magnetic interaction of the material, thereby opening a gateway to achieve nonlinear spin dynamics and high-bandwidth spintronic devices in a non-magnetic material.

II. RESULTS

A. Nonlinear nature of room-temperature defect-enabled spin amplification

The spin amplification in (Ga, N)As can be described by the following set of rate equations with the details given in Note 1 within the Supplemental Material [20,21],

$$\frac{d\vec{S}}{dt} = \vec{S}_0 - \vec{T} - \frac{\vec{S}}{\tau_s}, \quad (1.1)$$

$$\frac{d\vec{S}_c}{dt} = \vec{T} - \frac{\vec{S}_c}{\tau_{sc}}, \quad (1.2)$$

$$\frac{dn}{dt} = G - \frac{n}{\tau} + R. \quad (1.3)$$

Equations (1.1)–(1.3) describe the dynamics associated with conduction-electron spin \vec{S} , defect-electron spin \vec{S}_c , and conduction-electron density n under the condition of optical orientation [22]. The circularly polarized excitation generates initial spin and carriers to the conduction band (CB) with rates of \vec{S}_0 and G , followed by spin relaxation and annihilation of photocarriers with characteristic times of τ_s and τ . τ_{sc} is the spin-relaxation time of the defect electron. The essence of spin amplification is represented by spin-dependent recombination, as illustrated in Fig. 1(b), which is composed of (1) transfer of spin angular momentum $\vec{T} = \gamma_e(N\vec{S} - n\vec{S}_c)$ from the CB to the defect state via the spin-conserved capturing process; and (2) Pauli blockade correction to the nonradiative recombination rate, $R = 4\gamma_e\vec{S} \cdot \vec{S}_c$. Here, γ_e is the electron-capturing coefficient of the defect center. N is the density of available spin-filtering defect states. R takes positive (negative) values, and thus, inhibits (promotes) the nonradiative annihilation of the photocarriers when the conduction- and defect-electron

spins are parallel (antiparallel). The forms of \vec{T} and R suggest that such a defect-enabled spin-amplification process has an inherently nonlinear nature from the spin-carrier and spin-spin interactions.

To quantitatively assess the spin nonlinearity, we consider harmonic generation from an optical excitation with a modulated circular polarization at a given frequency ω_0 , as illustrated in Fig. 1(a). As a result, the time evolution of carrier and spin density in Eq. (1) needs to be considered as the series sum of the harmonics, e.g., $\vec{S}(t) = \sum_{\xi} \vec{S}^{(\xi)} e^{i\xi\omega_0 t}$ and $n(t) = \sum_{\xi} n^{(\xi)} e^{i\xi\omega_0 t}$. Here, superscript ξ denotes the order of the harmonics with frequency $\omega = \xi\omega_0$. \vec{T} and R then couple harmonics of different orders and drive the oscillation of the CB carrier and spin density at the corresponding frequencies. For instance, one can show that the CB-electron density develops second-order harmonics with magnitude

$$n^{(2)} = R^{(2)}\tau. \quad (2)$$

In the absence of an external magnetic field, the time evolution of the CB-electron spin density contains third-order harmonics with magnitude

$$\vec{S}^{(3)} = \vec{T}^{(3)}T_s^{\text{eff}}. \quad (3)$$

Here, T_s^{eff} is an effective spin lifetime for the CB electron. $R^{(2)} = 4\gamma_e\vec{S}^{(1)} \cdot \vec{S}_c^{(1)}$ and $\vec{T}^{(3)} = \gamma_e[N^{(2)}\vec{S}^{(1)} - n^{(2)}\vec{S}_c^{(1)}]$, showing that the higher-order harmonics are converted from the lower-order ones through the spin-dependent recombination process. Detailed derivations of Eqs. (2) and (3) can be found in Note 2 within the Supplemental Material [21]. To further demonstrate the harmonic generation of spin modulation in a room-temperature defect-enabled spin amplifier, we solve the full set of rate equations in the low-frequency limit. The time evolution of the CB carrier and spin density is converted into the frequency domain with fast Fourier transformation (FFT) and the results are shown in Fig. 1(c). The numerical simulations further confirm the emerging second- and fourth-order harmonics in $n(t)$, as well as the first- and third-order harmonics in $\vec{S}(t)$.

The conversion of low-frequency modulation of the spin signal to higher-harmonic oscillation of carriers and spin density is a direct consequence of spin-dependent recombination via the defect center. One may view the oscillation of the conduction-electron spin, \vec{S} , with given modulation frequency ω_0 as the new excitation of the system, i.e., $\vec{S}^{(1)}$. Since the oscillation of the defect-electron spin, \vec{S}_c , is received from the transfer of angular moment from the conduction electron to the defect center through the multiphonon-assisted spin-conserved capturing process, the spin-dependent recombination correction, R , in

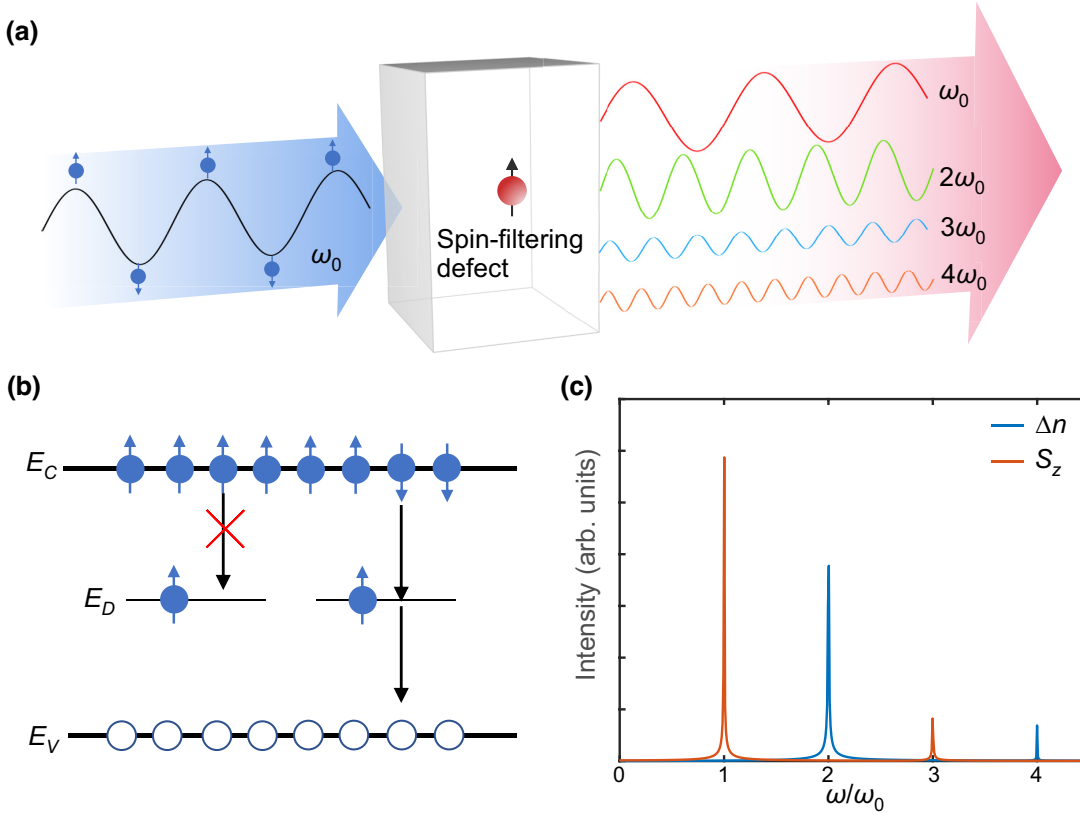


FIG. 1. Room-temperature defect-enabled harmonic generation of spin signal. (a) Schematic illustration of harmonic generation of a spin signal via spin-filtering defects. Harmonic generation is driven by modulation of the conduction-electron spin polarization at frequency ω_0 . (b) Schematic energy diagram of (Ga,N)As. Spin-dependent recombination via the spin-filtering defect is illustrated. (c) Simulation of the output frequency-domain spectra from (Ga,N)As for carrier density Δn and spin projection S_z .

Eq. (1.3) essentially bridges the interaction between quasi-particles. It naturally produces sum-frequency generation, which takes the two new excitations of $\hat{S}^{(1)}$, each with a quasiparticle energy of $\hbar\omega_0$, to a sum-frequency excitation, $n^{(2)}$, with an energy of $2\hbar\omega_0$. Other higher-order harmonics can be understood with a similar sum-frequency process through the same nonlinear term.

B. Spin-harmonic generation in a room-temperature defect-enabled spin amplifier

Harmonic generation from the modulated spin signal is then measured for a (Ga,N)As/QD nanostructure consisting of a 20-nm-thick (Ga,N)As layer tunneling coupled with InAs QDs. Schematic illustrations of the structure and band alignment of the studied sample are shown in Figs. 2(b) and 2(c). The steady-state photoluminescence (PL) spectra of the (Ga,N)As/QD nanostructure can be found in Fig. S1 within the Supplemental Material [21]. The choice of (Ga,N)As/QD for the demonstration of the proposed spin nonlinearity has several advantages. To begin with, efficient spin amplification and the record-high electron-spin polarization were recently demonstrated

in the same nanostructure as that used here [19]; this suggests stronger spin nonlinearity compared with a bare (Ga,N)As epilayer or a (Ga,N)As/GaAs quantum well structure. Additionally, owing to the complete removal of the heavy-hole and light-hole degeneracy in an InAs QD [19,23,24], the conduction-electron spin polarization can be directly converted into the circular polarization of the QD emission, which can be conveniently characterized with polarization-resolved optical spectroscopy.

The measurement scheme is shown in Fig. 2(a). Circular polarization of the excitation laser (780 nm) is modulated with an electro-optical amplitude modulator (EOAM) and PL emission from the sample is collected in the backscattering geometry. The choice of the excitation laser wavelength is to ensure optical orientation of GaAs conduction electrons, which are then transferred to the adjacent (Ga,N)As layer for spin amplification and nonlinear processes. The polarization optics decomposes the PL into σ^+ and σ^- components (I^{σ^+} and I^{σ^-}), which are then spectrally dispersed and detected with a liquid-nitrogen-cooled Ge detector. Both I^{σ^+} and I^{σ^-} are recorded as a function of time with an oscilloscope. The bandwidths of the Ge detector and oscilloscope are 20 kHz and 500 MHz,

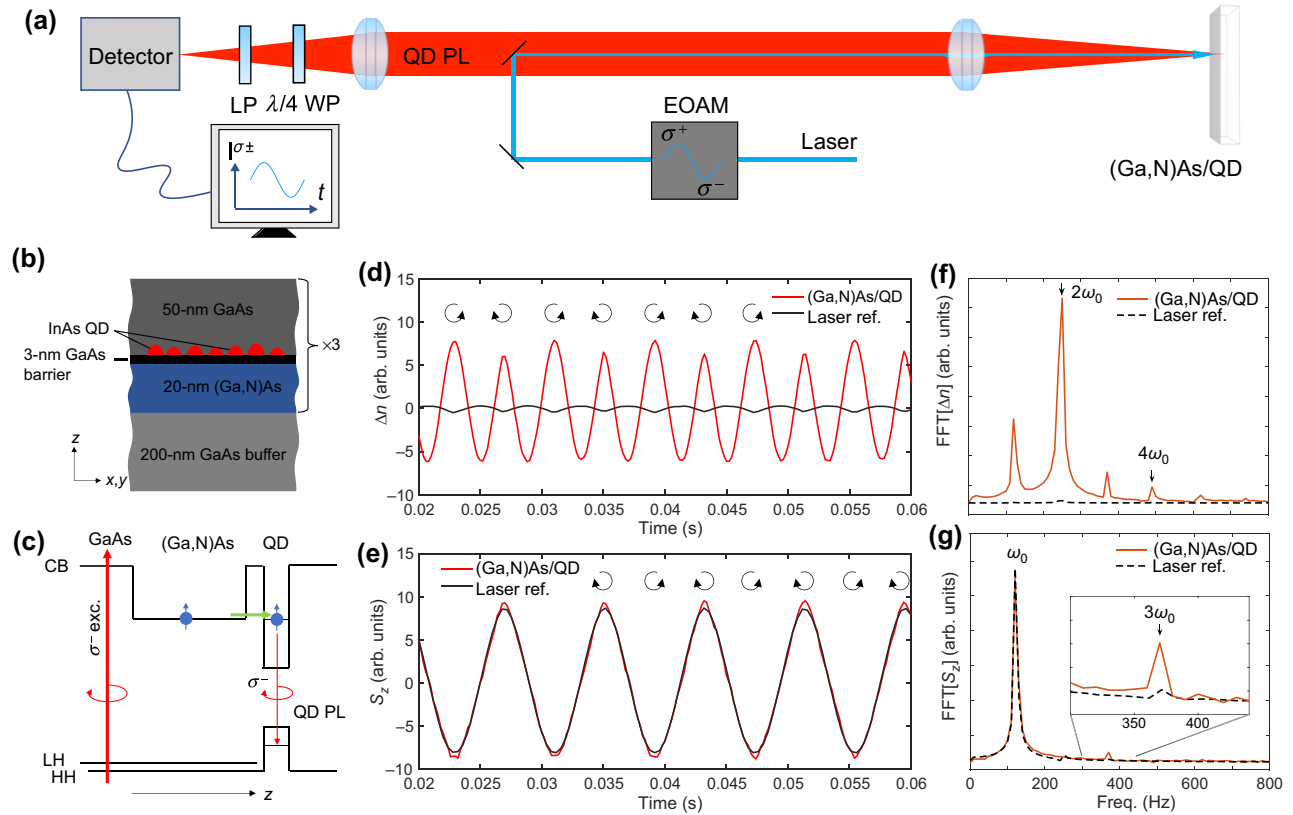


FIG. 2. Measurement schematics and nonlinear response from the (Ga,N)As/QDs. (a) Schematic illustration of the measurement scheme. EOAM is used to generate sinusoidal modulation of circular polarization of excitation laser, and the σ^+ and σ^- PL components of the emission are recorded as a function of time. Schematic structure (b) and band alignment (c) of the investigated (Ga,N)As/QDs sample. Measured (d) conduction-electron density, Δn , and (e) spin projection, S_z , as a function of time from the emission of the (Ga,N)As/QDs sample or reflected laser light. (f),(g) Corresponding FFT spectra from (d),(e). Close-up spectra of FFT[S_z] around $3\omega_0$ are shown in the inset of (g). Laser wavelength is fixed at 780 nm, and excitation power is kept constant at 100 mW.

respectively. The modulation frequency of the EOAM is kept low, at $\omega_0 = 123$ Hz, to avoid any instrumental distortion of the time-resolved signal caused by the slow detector. We note that all the measurements are performed by detecting the emission of the QD-exciton ground state at 1200 nm and at room temperature.

Figures 2(d) and 2(e) show typical time responses of the polarization-resolved PL from the (Ga,N)As/QDs under modulation of the excitation polarization. Here, the signal associated with CB-electron density, $n(t)$, and CB-electron spin projection, $S_z(t)$, are taken as $I^{\sigma^+} + I^{\sigma^-}$ and $(I^{\sigma^-} - I^{\sigma^+})/2$, respectively, according to the spin-selection rules [22]. Despite the excitation power being kept constant, the total PL intensity develops a strong undulation in $\Delta n(t)$. $\Delta n(t)$ reaches local maxima under both σ^+ - and σ^- -polarized excitation, indicating a dominant contribution from the second-order harmonics. On the other hand, $S_z(t)$ mainly follows the modulation of excitation polarization that is superimposed by higher-frequency components. The higher-order harmonics in $S_z(t)$ become obvious when compared with the reference signal recorded

from the reflected laser light (denoted as laser Ref.). In Figs. 2(f) and 2(g), we show the corresponding FFT of the obtained signal. FFT reveals the contribution of the first- and third-order harmonics in S_z and the second- and fourth-order harmonics in Δn , as predicted by the theory shown in Fig. 1(c). We note that odd-order harmonics are also observed for Δn , which are not explained by current theory, and are likely caused by either other nonlinear processes or a slight imbalance between the σ^+ - and σ^- -polarization components of the excitation or emission light clearly visible in Fig. 2(d) or both. The latter is discussed in more detail in Note 3 within the Supplemental Material, with the simulated results given in Fig. S2 within the Supplemental Material [21]. Despite this minor deviation, we show in Fig. S2 within the Supplemental Material [21] that the intended nonlinear response is not affected noticeably.

The observed harmonic generation from the spin modulation originates from spin-dependent recombination, which is expected to be highly dynamic. We thus repeat the measurements with various excitation-power levels, and the resulting FFT spectra for Δn and S_z are plotted

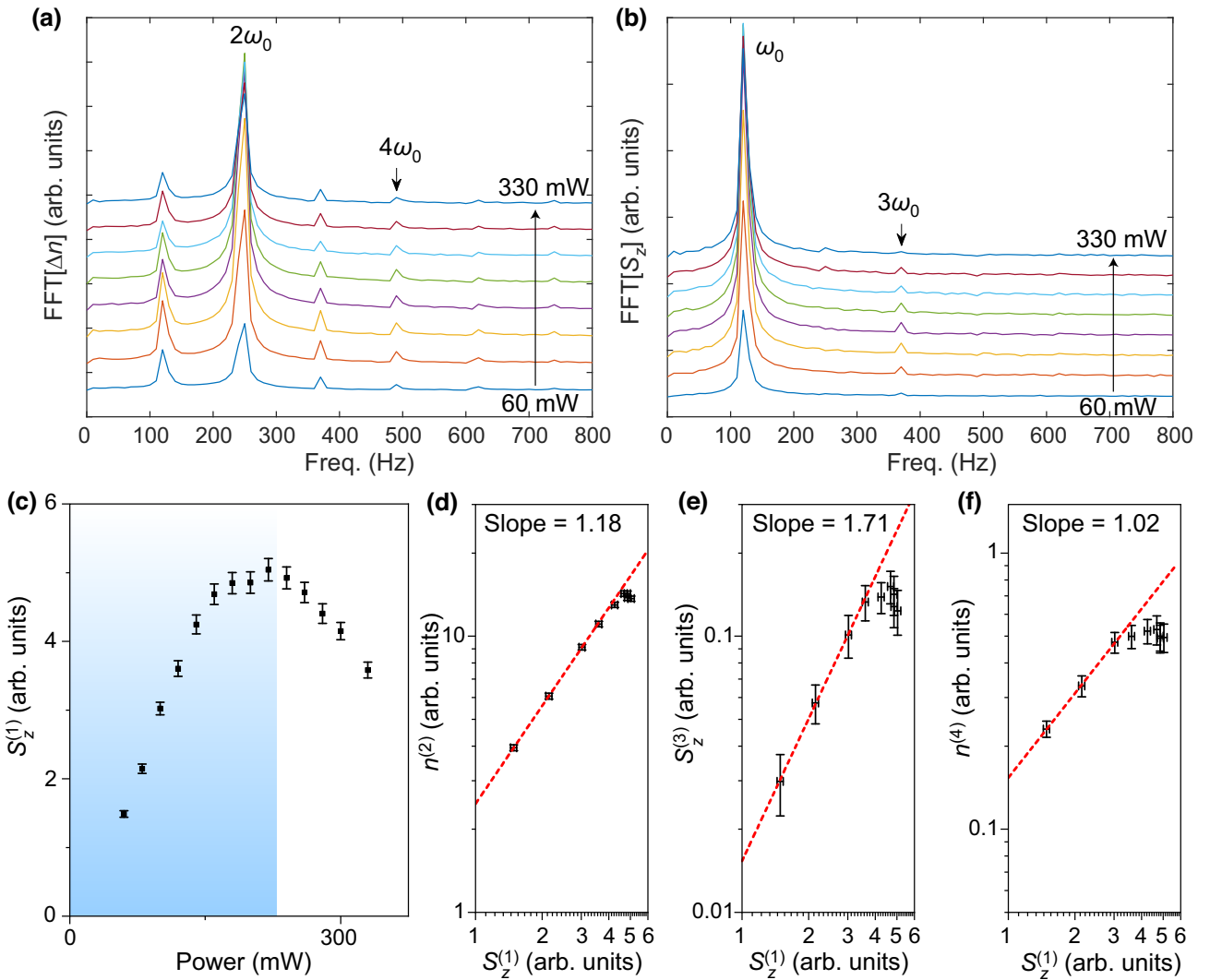


FIG. 3. Power dependence of the nonlinear response. FFT of (a) conduction-electron density, Δn , and (b) spin projection, S_z , at various excitation-power levels. (c) Magnitude of the conduction-electron spin projection, $S_z^{(1)}$, as a function of excitation power. (d)–(f) Magnitudes of higher-order harmonics $n^{(2)}$, $S_z^{(3)}$, and $n^{(4)}$, respectively, plotted as a function of $S_z^{(1)}$ over the shaded power range in (c), where $S_z^{(1)}$ monotonously increases with increasing excitation power. Dashed lines are the linear fitting of data in the log-log plots with the specified fitting parameters for the slope.

in Figs. 3(a) and 3(b). The harmonic generation gives rise to resonances in the FFT spectra. The magnitudes of corresponding harmonics $n^{(\xi)}$ and $S_z^{(\xi)}$ are extracted from fitting with a Lorentzian line shape. In Fig. 3(c), the obtained $S_z^{(1)}$ is plotted against the excitation power. $S_z^{(1)}$ is found to increase with increasing excitation power within the weak-power regime, but at a higher excitation power it starts to saturate and eventually decreases at a further higher power. The power dependence of $S_z^{(1)}$ fits the typical behavior of the defect-enabled spin amplification, which is deactivated as the defect state is occupied by two electrons of opposite spins in a spin-paired-off state at a high pumping fluence [25]. Next, the higher-order harmonics generated from the spin nonlinearity, e.g., $n^{(2)}$, $S_z^{(3)}$, and $n^{(4)}$, are plotted against $S_z^{(1)}$ in Figs. 3(d)–3(f), respectively, by taking

data from the shaded power range in Fig. 3(c), where a monotonous increase of $S_z^{(1)}$ with the excitation power is found. The higher-order harmonics show a monotonous growth with $S_z^{(1)}$ until saturation is reached. A linear fit of the log-log plots of Figs. 3(d) and 3(e) yields a slope of 1.18 and 1.71 for $n^{(2)}$ and $S_z^{(3)}$, respectively. We note that the obtained power factors for $n^{(2)}$ and $S_z^{(3)}$ deviate from the values that one may expect for the second- and third-order nonlinear processes [26,27]. This is understandable since the variation of $S_z^{(1)}$ is less than 1 order of magnitude, and the scaling of the nonlinear power law is largely compromised when $S_z^{(1)}$ is close to saturation. Nevertheless, the observation of the superlinear dependence confirms the nonlinear nature of the observed harmonic generation. In Fig. 3(f) the fourth-order process is seen to saturate much

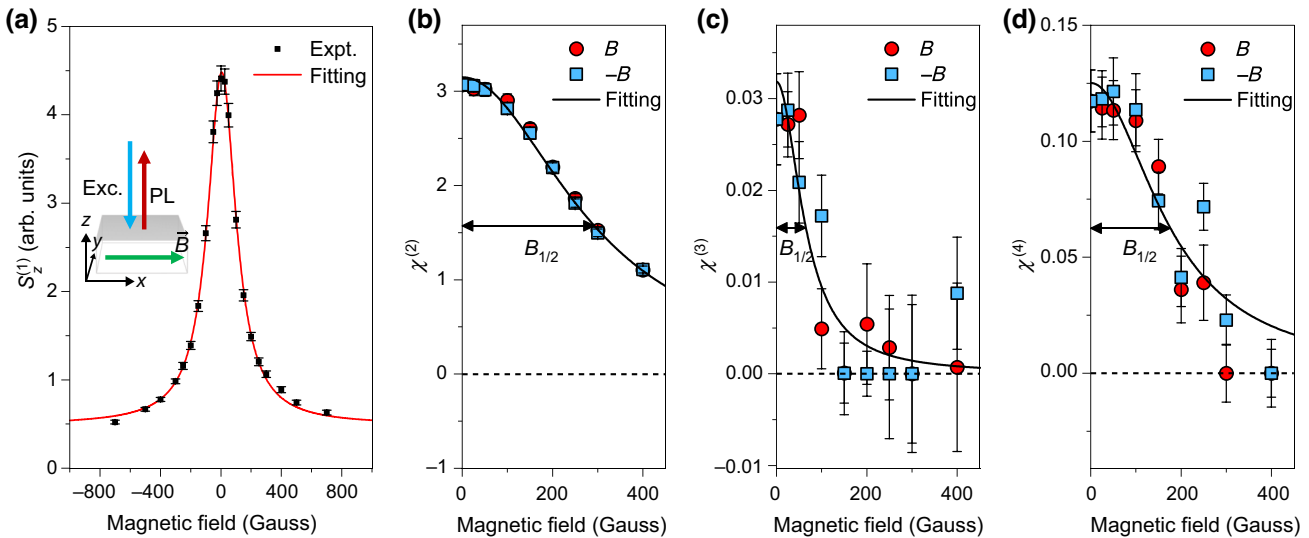


FIG. 4. Control of the nonlinear response by a magnetic field. (a) $S_z^{(1)}$ measured as a function of a transverse magnetic field. Experimental data are fitted by a Lorentzian function. Inset illustrates the measurement geometry. As-measured nonlinear coefficients (b) $\chi^{(2)}$, (c) $\chi^{(3)}$, and (d) $\chi^{(4)}$ as a function of the transverse magnetic field along the positive (B) and negative ($-B$) field directions, as marked by red filled circles and blue filled squares, respectively. Lorentzian fittings of experimental data are given by solid lines, and half widths of the fittings, $B_{1/2}$, are marked with arrows.

earlier than those of $n^{(2)}$ and $S_z^{(3)}$, and the power factor is found to be closer to 1.

C. Control of nonlinear-spin response by a magnetic field

Being able to control the harmonic generation adds flexibility to potential applications exploiting nonlinearity. Tunable harmonic generation is achieved in optical nonlinear material through control of the symmetry-breaking effect or resonance shifting [28–31]. In a magnetic nonlinear system, spin dynamics and a nonlinear response can be altered by a magnetic field [11,12]. Here, we show that the observed nonlinear spin response of the (Ga, N)As/QD nanostructure can also be conveniently tuned by applying a transverse magnetic field, as shown in the inset of Fig. 4(a). It is understood that a small transverse magnetic field depolarizes the defect-electron spin and, as a result, suppresses spin amplification via the defect states [25]. This is observed in Fig. 4(a), where as-measured $S_z^{(1)}$ decreases with an increase of the applied field strength. Fitting the magnetic field dependence of $S_z^{(1)}$ with a Lorentzian function yields a half width of $B_{1/2} = 113.8$ G, corresponding to a defect-spin lifetime of 499.6 ps [25]. To avoid interference of the magnetic field dependence of $S_z^{(1)}$ and focus solely on the nonlinear response, we define a set of dimensionless nonlinear coefficients by dividing the higher-order harmonics by $S_z^{(1)}$:

$$\chi^{(2)} = \frac{n^{(2)}}{S_z^{(1)}}, \quad \chi^{(3)} = \frac{S_z^{(3)}}{S_z^{(1)}}, \quad \chi^{(4)} = \frac{n^{(4)}}{S_z^{(1)}}. \quad (4)$$

Figures 4(b)–4(d) show the extracted nonlinear coefficient $\chi^{(\xi)}$ ($\xi = 2, 3, 4$) as a function of magnetic field strength. The results for both positive and negative field (denoted as B and $-B$) are shown. In all three cases, $\chi^{(\xi)}$ decreases with increasing magnetic field strength, suggesting that not only the spin amplification but also the proposed spin nonlinearity can be tuned by a magnetic field in the room-temperature spin amplifier.

The magnetic field dependence of $\chi^{(\xi)}$ differs for nonlinear processes of different orders. The half width, $B_{1/2}$, of the magnetic field dependence of $\chi^{(\xi)}$, as measured by fitting to the Lorentzian function, has the largest and smallest values for $\chi^{(2)}$ and $\chi^{(3)}$, respectively. Smaller $B_{1/2}$ indicates that the corresponding nonlinear process is more sensitive to the applied magnetic field. The difference of the magnetic field response is determined by the subtle difference of the spin dynamics in the presence of a magnetic field.

For an in-depth understanding of the magnetic field tuneability in the spin-harmonic generation, we resort to numerical simulations with the full set of coupled rate equations. Figure 5(a) shows the simulation results of the higher-order harmonics ($n^{(2)}$, $S_z^{(3)}$, and $n^{(4)}$) as a function of $S_z^{(1)}$. All the simulation parameters, e.g., defect concentration, capture coefficients, and spin-relaxation time, are listed in Fig. S3 and Table S1 within the Supplemental Material [21]. They are comparable with the values used in previous reports [18,19]. The simulation shows satisfactory agreement with the experimental results. First of all, both $n^{(2)}$ and $S_z^{(3)}$ exhibit a superlinear dependence on $S_z^{(1)}$ before saturation is reached. Over a large span of $S_z^{(1)}$,

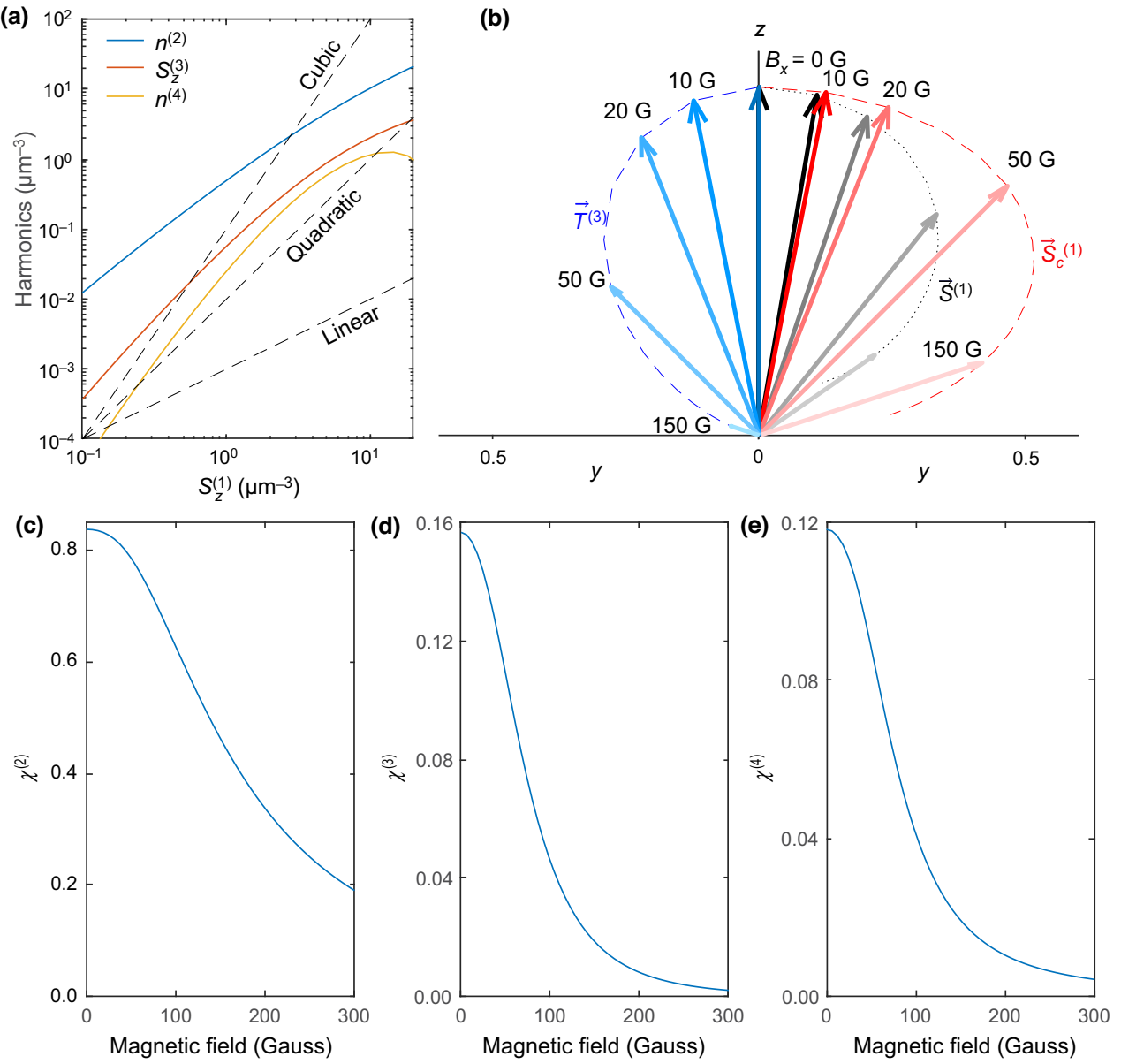


FIG. 5. Simulations of the nonlinear spin response in a defect-enabled spin amplifier. (a) Simulations of higher-order harmonics $n^{(2)}$, $S_z^{(3)}$, and $n^{(4)}$ as a function of $S_z^{(1)}$. Dashed lines are guidelines for linear, quadratic, and cubic dependence. (b) Simulations of the conduction and defect spin vector ($\vec{S}^{(1)}$ and $\vec{S}_c^{(1)}$) as well as the third-order spin-transfer vector, $\vec{T}^{(3)}$, in the presence of a finite transverse magnetic field, B_x . (c)–(e) Simulated nonlinear coefficients $\chi^{(2)}$, $\chi^{(3)}$, and $\chi^{(4)}$, respectively, as a function of applied magnetic field.

the power factors of $n^{(2)}$ and $S_z^{(3)}$ are around 1–2, which are comparable to the measured values shown in Figs. 3(d) and 3(e). In Fig. S4 within the Supplemental Material [21], we show that the power factors of $n^{(2)}$, $S_z^{(3)}$, and $n^{(4)}$ eventually approach 2, 3, and 4, respectively, as $S_z^{(1)}$ decreases further away from the saturation point. Furthermore, much earlier saturation is found for $n^{(4)}$, which is also experimentally observed in Fig. 3(f). Both the experimental results and theory confirm that the proposed spin nonlinearity is highly dynamic and the nonlinear coefficients are altered between different dynamic regimes.

The magnetic field dependence of nonlinear coefficients $\chi^{(\xi)}$ are computed and shown in Figs. 5(c)–5(e) for $\xi = 2$, 3, and 4, respectively. The simulation results fit qualitatively well with the experiments; the half width, $B_{1/2}$, derived from the magnetic field dependence is largest for $\chi^{(2)}$ and smallest for $\chi^{(3)}$. The second-order nonlinearity scales with $R^{(2)}$, which is essentially the product of the conduction- and defect-electron spins. $\chi^{(2)}$ is therefore proportional to the projection of the defect-electron spin, $\vec{S}_c^{(1)}$, onto the conduction-electron spin, $\vec{S}^{(1)}$. In the presence of a finite transverse magnetic field, B_x , both $\vec{S}_c^{(1)}$ and

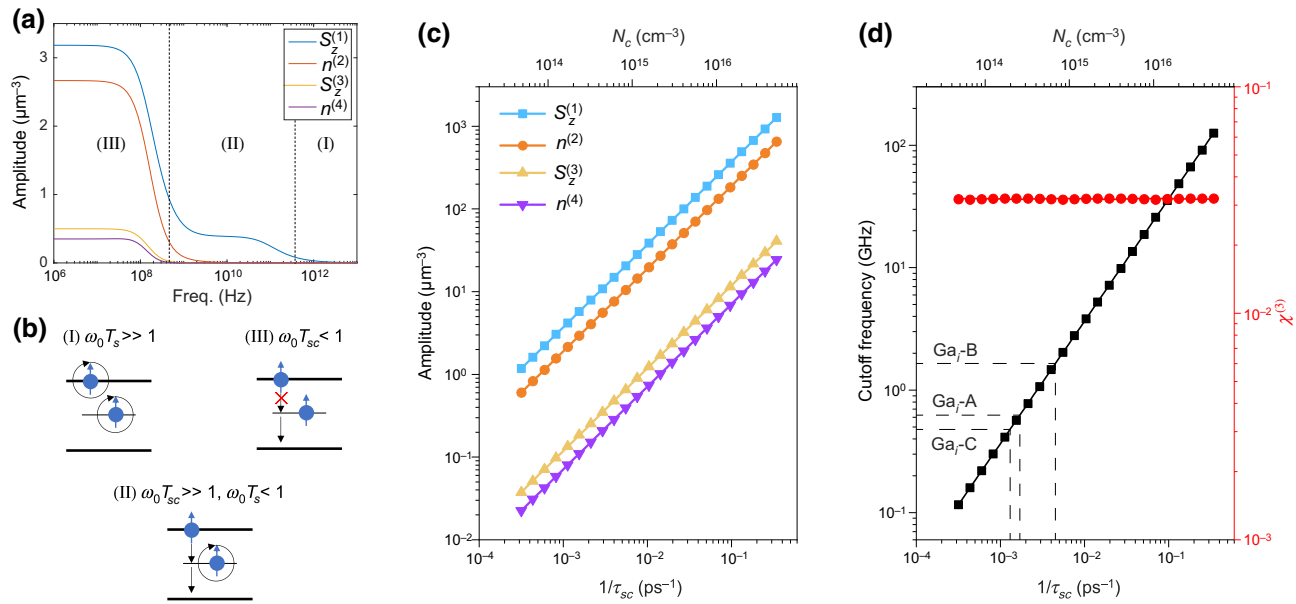


FIG. 6. Nonlinear operation speed. (a) Simulations of the amplitude of different harmonics as a function of operation frequency. (b) Conduction- and defect-electron-spin configuration in three characteristic regimes of the operation frequency marked in (a). ω_0 is the operation frequency. T_s and T_{sc} are the spin lifetimes of conduction and defect electrons, with $T_{sc} > T_s$. (c),(d) Simulations of the amplitude of different harmonics, cutoff frequency ω_c , and $\chi^{(3)}$ as a function of defect electron-spin relaxation rate, τ_{sc}^{-1} . Required defect concentration, N_c , is scaled linearly with $\tau_{sc}^{-1} \cdot \tau_{sc}^{-1}$ values for three types of spin-filtering defects found in (Ga, N)As are marked in (d).

$\vec{S}^{(1)}$ tilt away from the z axis and eventually get balanced by competition between spin precession and spin relaxation. As illustrated in the right part of Fig. 5(b), $\chi^{(2)}$ then decreases in the magnetic field as $\vec{S}_c^{(1)}$ is depolarized and rotated away from $\vec{S}^{(1)}$. On the other hand, $\chi^{(3)}$ is associated with $\vec{T}^{(3)}$, which is depolarized and tilted away from the z axis at a much smaller B_x as compared to $\vec{S}_c^{(1)}$ or $\vec{S}^{(1)}$ as shown in the left part of Fig. 5(b). This explains the observed sensitive magnetic field dependence of $\chi^{(3)}$.

An alternative way of controlling the room-temperature spin amplifier is by applying a longitudinal magnetic field in a Faraday geometry. In such a configuration, the magnetic field causes the Zeeman splitting of the defect-electron-spin levels, which then competes with the hyperfine spin-relaxation mechanism, leading to an enhancement of spin amplification in the field. The effect was explored earlier in (Ga, N)As bulk material [32]. However, in the (Ga, N)As/QD nanostructure studied here, the change of the spin amplification, as probed by the steady-state QD PL polarization, is less than 5% over a magnetic field range of 1 T (see Fig. S5 within the Supplemental Material [21]), which is considerably less effective than the Voigt geometry and is therefore not considered for spin-nonlinearity control in the current work.

D. Speed of the spin-nonlinearity operation

The observed spin nonlinearity in the room-temperature defect-enabled spin amplifier can be potentially tailored for

spintronic device applications. The operation speed of such a nonlinear spintronic device is expected to be much faster than the modulation frequency used in our measurement, which is mainly limited by the instrumental response. Figure 6(a) shows the magnitude of harmonic generation simulated as a function of the modulation frequency, ω_0 , of the input spin signal. The nonlinear response is found to decrease with increasing operation speed, which exhibits three-stage behavior. In Fig. 6(b), we assign the three stages to three distinct regimes of spin dynamics for the CB and defect electrons. In stage I, the high-frequency regime, $\omega_0 T_{sc} \gg 1$ and $\omega_0 T_s \gg 1$, where T_s (T_{sc}) is the spin lifetime of the CB (defect) electron. In this case, neither the CB- nor defect-electron spin can follow the input spin modulation, which yields a vanishing $S_z^{(1)}$ and higher-order harmonics. In stage II, the intermediate-frequency regime, $\omega_0 T_{sc} \gg 1$ and $\omega_0 T_s < 1$. In this regime, the CB-electron spin can now follow the input spin signal, whereas the defect-electron spin cannot. As a result, $S_z^{(1)}$ has a small but finite value, while the nonlinear response and higher-order harmonics are not activated yet. In stage III, the low-frequency regime, $\omega_0 T_{sc} < 1$ and $\omega_0 T_s < 1$, when both CB- and defect-electron spins can follow the modulation speed. Spin-dependent recombination via the defect states is therefore activated, leading to a drastic enhancement of $S_z^{(1)}$ and emergence of higher-order harmonics, as shown in Fig. 6(a). We define the nonlinear operation speed with cutoff frequency ω_c at which the amplitude of the corresponding harmonics, e.g., $S_z^{(3)}$, drops by 3 dB

from the maximum value. For instance, in the simulation of Fig. 6(a), ω_c for the third-order nonlinear process is found to be about 0.1 GHz.

The simulation shows that spin nonlinearity and spin amplification are turned on simultaneously when the spin lifetimes of both CB and defect electrons become shorter than the time needed for the operation, i.e., $T_{sc}, T_s < 1/\omega_0$. The key to improving the nonlinear operation speed is therefore to reduce the corresponding spin lifetime. T_{sc} and T_s are determined by both the corresponding spin-relaxation time (τ_{sc} and τ_s) and effective lifetime. To facilitate optimization of the spin amplification and nonlinearity throughout the parametric space, we consider the dynamic regime with $\tau_{sc}^{-1} \ll \tau_s^{-1} \ll \gamma_e N_c$ by fixing the ratio of $\tau_{sc}^{-1}/\tau_s^{-1} = \tau_s^{-1}/\gamma_e N_c = 0.1$. Here, N_c is the total concentration of spin-filtering defects. This is a necessary condition to activate spin-dependent recombination and spin amplification. We note that such a condition is always possible to reach, since the spin-relaxation mechanism of CB electrons and defect concentration can be tuned independently by designing the material parameters (such as chemical composition and codoping) and growth methods and conditions [molecular beam epitaxy (MBE) versus chemical vapor deposition, gas-source versus solid-source MBE, growth temperature, etc.]. With the proper choice of excitation power, e.g., by scaling $G = \gamma_G^{-1} \tau_{sc}^{-2}$, one can show that both cutoff frequency ω_c and the harmonic generation of arbitrary order ($n^{(\xi)}$ and $S_z^{(\xi)}$) increase linearly with an increase of τ_{sc}^{-1} (see Note 4 within the Supplemental Material [21]):

$$\omega_c, n^{(\xi)}, S_z^{(\xi)} \propto \tau_{sc}^{-1}. \quad (5)$$

The scaling rule is confirmed by the numerical simulation shown in Figs. 6(c) and 6(d), taking $\gamma_G = 10^{-6} \mu\text{m}^3 \text{ ps}^{-1}$. It suggests that high operation speed and prominent harmonics generation with the modulated spin signal can be achieved simultaneously by shortening τ_{sc} . Generally speaking, τ_{sc} depends on spin-relaxation mechanism and can vary over orders of magnitude for different defect centers [25,33–36]. Specifically, the defect states responsible for spin amplification in (Ga, N)As is an interstitial defect, Ga_i^{2+} [25]. Spin relaxation of Ga_i^{2+} is governed by the central hyperfine interaction, and τ_{sc} is found to vary from 220 to 800 ps, depending on the hyperfine-coupling strength with the nuclear spin of defect Ga_i^{2+} that differs between different configurations of Ga_i^{2+} . In Fig. 6(d), the reported τ_{sc}^{-1} values for the different Ga_i^{2+} in (Ga, N)As (Ga_i -A, Ga_i -B, and Ga_i -C) are marked. For Ga_i -B, a nonlinear operation frequency exceeding 1 GHz with a decent $\chi^{(3)}$ is readily achievable. More importantly, the required Ga_i^{2+} defect concentration is on the order of about 10^{15} cm^{-3} , which is among the typically reported values for (Ga, N)As with N compositions of 1%–1.5%. We note

that an even higher nonlinear operation speed will be possible if new defect centers with a shorter spin-relaxation time can be found. The scaling rule of Eq. (5) therefore serves as a guideline for the rational design of nonlinear spin devices based on the proposed mechanism.

III. CONCLUSIONS

We theoretically propose and experimentally demonstrate the emergence of a nonlinear spin response from a room-temperature defect-enabled spin amplifier. The spin nonlinearity originates from the defect-mediated spin-dependent recombination, which is distinctly different from, but complementary to, the nonlinear effect found in magnetic materials that require strong magnetic interactions. The spin nonlinearity converts the input polarization modulation to the higher-order harmonic oscillations of the CB electron and spin density. We further show that such spin-harmonic generation can be controlled conveniently by an external magnetic field. The demonstrated spin nonlinearity can readily operate at a frequency exceeding 1 GHz in the studied (Ga, N)As/InAs nanostructure. Furthermore, we provide a guideline for the rational design and optimization of the proposed spin nonlinearity in non-magnetic semiconductors with simultaneously achievable higher operation speed and nonlinear response, which may help to extend the functionality of current semiconductor-based electronic and photonic technologies.

ACKNOWLEDGMENTS

Y.H. acknowledges financial support from the Knut and Alice Wallenberg Foundation (Grant No. KAW 2020.0029); W.M.C. acknowledges financial support from the Swedish Research Council (Grant No. 2020-04530); I.A.B. acknowledges financial support from the Swedish Research Council (Grant No. 2019-04312); and W.M.C. and I.A.B. acknowledge financial support from the Swedish Government Strategic Research Area in Materials Science on Functional Materials at Linköping University (Faculty Grant SFO-Mat-LiU No. 2009-00971). V.P., A.A., R.I., T.H., and M.G. acknowledge financial support from the Academy of Finland projects NanoLight (No. 310985) and QuantSi (No. 323989) and the ERC Advanced Grant AMETIST (No. 695116).

-
- [1] E. Garmire, Nonlinear optics in daily life, *Opt. Express* **21**, 30532 (2013).
 - [2] G. Li, S. Zhang, and T. Zentgraf, Nonlinear photonic metasurfaces, *Nat. Rev. Mater.* **2**, 17010 (2017).
 - [3] O. Reshef, I. De Leon, M. Z. Alam, and R. W. Boyd, Non-linear optical effects in epsilon-near-zero media, *Nat. Rev. Mater.* **4**, 535 (2019).
 - [4] S. Ghimire and D. A. Reis, High-harmonic generation from solids, *Nat. Phys.* **15**, 10 (2019).

- [5] L. Fan, X. Yan, H. Wang, and L. V. Wang, Real-time observation and control of optical chaos, *Sci. Adv.* **7**, 1 (2021).
- [6] Q. Ma, *et al.*, Observation of the nonlinear Hall effect under time-reversal-symmetric conditions, *Nature* **565**, 337 (2019).
- [7] T. Ideue and Y. Iwasa, Symmetry breaking and nonlinear electric transport in van der Waals nanostructures, *Annu. Rev. Condens. Matter Phys.* **12**, 201 (2021).
- [8] J. E. Greenwald, J. Cameron, N. J. Findlay, T. Fu, S. Gunasekaran, P. J. Skabara, and L. Venkataraman, Highly nonlinear transport across single-molecule junctions via destructive quantum interference, *Nat. Nanotechnol.* **16**, 313 (2021).
- [9] Z. Yang, S. Zhang, and Y. C. Li, Chaotic Dynamics of Spin-Valve Oscillators, *Phys. Rev. Lett.* **99**, 134101 (2007).
- [10] I. Barsukov, H. K. Lee, A. A. Jara, Y.-J. Chen, A. M. Gonçalves, C. Sha, J. A. Katine, R. E. Arias, B. A. Ivanov, and I. N. Krivorotov, Giant nonlinear damping in nanoscale ferromagnets, *Sci. Adv.* **5**, 1 (2019).
- [11] S. Baierl, J. H. Mentink, M. Hohenleutner, L. Braun, T.-M. Do, C. Lange, A. Sell, M. Fiebig, G. Woltersdorf, T. Kampfrath, and R. Huber, Terahertz-Driven Nonlinear Spin Response of Antiferromagnetic Nickel Oxide, *Phys. Rev. Lett.* **117**, 197201 (2016).
- [12] M. Hudl, M. D'Aquino, M. Pancaldi, S.-H. Yang, M. G. Samant, S. S. P. Parkin, H. A. Dürr, C. Serpico, M. C. Hoffmann, and S. Bonetti, Nonlinear Magnetization Dynamics Driven by Strong Terahertz Fields, *Phys. Rev. Lett.* **123**, 197204 (2019).
- [13] R. Cheng, D. Xiao, and A. Brataas, Terahertz Antiferromagnetic Spin Hall Nano-Oscillator, *Phys. Rev. Lett.* **116**, 207603 (2016).
- [14] S. S. Dhillon, *et al.*, The 2017 terahertz science and technology roadmap, *J. Phys. D: Appl. Phys.* **50**, 043001 (2017).
- [15] T. Jungwirth, X. Marti, P. Wadley, and J. Wunderlich, Antiferromagnetic spintronics, *Nat. Nanotechnol.* **11**, 231 (2016).
- [16] A. R. Mellnik, J. S. Lee, A. Richardella, J. L. Grab, P. J. Mintun, M. H. Fischer, A. Vaezi, A. Manchon, E.-A. Kim, N. Samarth, and D. C. Ralph, Spin-transfer torque generated by a topological insulator, *Nature* **511**, 449 (2014).
- [17] L. Šmejkal, Y. Mokrousov, B. Yan, and A. H. MacDonald, Topological antiferromagnetic spintronics, *Nat. Phys.* **14**, 242 (2018).
- [18] S. Chen, Y. Huang, D. Visser, S. Anand, I. A. Buyanova, and W. M. Chen, Room-temperature polarized spin-photon interface based on a semiconductor nanodisk-in-nanopillar structure driven by few defects, *Nat. Commun.* **9**, 3575 (2018).
- [19] Y. Huang, V. Polojärvi, S. Hiura, P. Höjer, A. Aho, R. Isoaho, T. Hakkarainen, M. Guina, S. Sato, J. Takayama, A. Murayama, I. A. Buyanova, and W. M. Chen, Room-temperature electron spin polarization exceeding 90% in an opto-spintronic semiconductor nanostructure via remote spin filtering, *Nat. Photonics* **15**, 475 (2021).
- [20] E. L. Ivchenko, V. K. Kalevich, A. Y. Shiryaev, M. M. Afanasiev, and Y. Masumoto, Optical orientation and spin-dependent recombination in GaAsN alloys under continuous-wave pumping, *J. Phys.: Condens. Matter* **22**, 465804 (2010).
- [21] See the Supplemental Material at <http://link.aps.org-supplemental/10.1103/PhysRevApplied.19.064048> for structure and energy alignment of the (Ga, N)As/QD sample; simulations of the nonlinear spin response under nonideal conditions; schematic energy diagram and dynamic parameters of the rate equation; simulations of the scaling law of the higher-order harmonics; QD emission polarization, P_{PL} , as function of applied longitudinal magnetic field in the Faraday geometry; simulation parameters of the nonlinear response; full rate-equation simulations of the spin nonlinearity in a room-temperature defect-enabled spin amplifier; derivation of Eqs. (2) and (3); simulations of the nonlinear spin response under nonideal conditions; and scaling of the rate equation.
- [22] F. Meier and B. P. Zakharchenya, *Optical Orientation* (North Holland, Amsterdam, 1984).
- [23] J. H. Blokland, F. J. P. Wijnen, P. C. M. Christianen, U. Zeitler, J. C. Maan, P. Kailuweit, D. Reuter, and A. D. Wieck, Hole levels in InAs self-assembled quantum dots, *Phys. Rev. B* **75**, 233305 (2007).
- [24] M. H. Ya, Y. F. Chen, and Y. S. Huang, Nonlinear behaviors of valence-band splitting and deformation potential in dilute GaN_xAs_{1-x} alloys, *J. Appl. Phys.* **92**, 1446 (2002).
- [25] Y. Puttisong, I. A. Buyanova, A. J. Ptak, C. W. Tu, L. Geelhaar, H. Riechert, and W. M. Chen, Room-temperature electron spin amplifier based on Ga(In)NAs alloys, *Adv. Mater.* **25**, 738 (2013).
- [26] M. R. Shcherbakov, H. Zhang, M. Tripepi, G. Sartorello, N. Talisa, A. AlShafey, Z. Fan, J. Twardowski, L. A. Krivitsky, A. I. Kuznetsov, E. Chowdhury, and G. Shvets, Generation of even and odd high harmonics in resonant metasurfaces using single and multiple ultra-intense laser pulses, *Nat. Commun.* **12**, 4185 (2021).
- [27] C. K. Ha, K. H. Nam, and M. S. Kang, Efficient harmonic generation in an adiabatic multimode submicron tapered optical fiber, *Commun. Phys.* **4**, 173 (2021).
- [28] J. Wang, N. Han, Z.-D. Luo, M. Zhang, X. Chen, Y. Liu, Y. Hao, J. Zhao, and X. Gan, Electrically tunable second harmonic generation in atomically thin ReS_2 , *ACS Nano* **16**, 6404 (2022).
- [29] K. Yao, *et al.*, Enhanced tunable second harmonic generation from twistable interfaces and vertical superlattices in boron nitride homostructures, *Sci. Adv.* **7**, 1 (2021).
- [30] I. Abdelwahab, B. Tilman, Y. Wu, D. Giovanni, I. Verzhbitskiy, M. Zhu, R. Berté, F. Xuan, L. D. S. Menezes, G. Eda, T. C. Sum, S. Y. Quek, S. A. Maier, and K. P. Loh, Giant second-harmonic generation in ferroelectric NbO_2 , *Nat. Photonics* **16**, 644 (2022).
- [31] H. Hong, *et al.*, Giant enhancement of optical nonlinearity in two-dimensional materials by multiphoton-excitation resonance energy transfer from quantum dots, *Nat. Photonics* **15**, 510 (2021).
- [32] Y. Puttisong, X. J. Wang, I. A. Buyanova, L. Geelhaar, H. Riechert, A. J. Ptak, C. W. Tu, and W. M. Chen, Efficient room-temperature nuclear spin hyperpolarization of a defect atom in a semiconductor, *Nat. Commun.* **4**, 1751 (2013).

- [33] A. Gottscholl, M. Diez, V. Soltamov, C. Kasper, A. Sperlich, M. Kianinia, C. Bradac, I. Aharonovich, and V. Dyakonov, Room temperature coherent control of spin defects in hexagonal boron nitride, [Sci. Adv. **7**, 1 \(2021\)](#).
- [34] X. Linpeng, M. L. K. Viitaniemi, A. Vishnuradhan, Y. Kozuka, C. Johnson, M. Kawasaki, and K.-M. C. Fu, Coherence Properties of Shallow Donor Qubits in ZnO, [Phys. Rev. Appl. **10**, 064061 \(2018\)](#).
- [35] T. de Guillebon, B. Vandolet, J.-F. Roch, V. Jacques, and L. Rondin, Temperature dependence of the longitudinal spin relaxation time T_1 of single nitrogen-vacancy centers in nanodiamonds, [Phys. Rev. B **102**, 165427 \(2020\)](#).
- [36] G. Garcia-Arellano, F. Bernardot, G. Karczewski, C. Testelin, and M. Chamarro, Spin relaxation time of donor-bound electrons in a CdTe quantum well, [Phys. Rev. B **99**, 235301 \(2019\)](#).